

Embedded 3D printing of Multi-material composites

Shitong Zhou (✉ s.zhou18@imperial.ac.uk)

Imperial College London <https://orcid.org/0000-0001-6366-5817>

Iuliia S Tirichenko

Imperial College London

Xun Zhang

University of Manchester

Yinglun Hong

Imperial College London

Harry Payne

Imperial College London

Philip Withers

The University of Manchester <https://orcid.org/0000-0002-6896-0839>

Florian Bouville

Imperial College London <https://orcid.org/0000-0002-1527-5045>

Eduardo Saiz

Imperial College London

Article

Keywords: Direct Ink Writing, rheology, microfluid device, ceramics with auxetic structure

Posted Date: October 19th, 2022

DOI: <https://doi.org/10.21203/rs.3.rs-2151613/v1>

License:   This work is licensed under a Creative Commons Attribution 4.0 International License.

[Read Full License](#)

Abstract

Additive manufacturing could open new opportunities in the design and fabrication of advanced composites and devices incorporating multiple phases. However, when it comes to the combination of inorganic materials (ceramics and metals) it is difficult to achieve the degree of structural control demanded by many advanced applications. To address this challenge, we have developed a means of embedded printing to build complex, fine structures within dense ceramics. We have formulated a self-healing ceramic gel that enables the movement of a printing nozzle in its interior and that heals without defect after it has passed. Upon subsequent heat treatment, the gel forms a dense, defect-free ceramic that encapsulates the printed structure. We demonstrate the potential of the technique through two case studies. One is the printing of light, sacrificial graphite structures to introduce complex microchannel arrangements in a ceramic for applications such as thermal management. The other is to embed dense steel framework structures in aluminum oxide to increase its fracture resistance. The approach enables the introduction of auxetic structures that generate works of fracture 50% greater than those obtained with simple fibre arrays and that are orders of magnitude above the fracture energy of the ceramic. These results suggest that embedded 3D printing can open the way to implement new designs in ceramic matrix composites.

Introduction

The attractive properties of ceramic materials such as high strength, hardness, good thermal stability and oxidation resistance make them the ideal candidates for many applications, particularly those involving exposure to demanding environments. However, the same properties that make ceramics so appealing render their machining and shaping particularly challenging.^{1–4} In addition, high performance demands a reliable control of the material architecture from the nano-level upwards and often requires the combination of several phases in a single structure. Perhaps nowhere is this more evident than in the need to enhance the fracture resistance of ceramics for highly-demanding structural applications. This need has triggered a significant research effort in the field of ceramic composites that goes from the more established methodologies of using fibre and particulate reinforcements to new approaches that look at the structural motifs in natural materials for inspiration. Additive manufacturing could help answer these challenges by opening up new avenues for the fabrication of ceramic structures and devices with bespoke geometries and unique architectures.

The term “additive manufacturing (AM)” (also known as 3D printing) encompasses a broad set of techniques by which objects are built up layer by layer according to a computer-aided design (CAD).^{5–8} These techniques are now applied to a wide range of materials including metals, ceramics and polymers. This design flexibility, and the ability to implement hierarchical microstructures, make the additive manufacturing of ceramics particularly interesting. Several AM techniques (binder jetting, selective laser melting, stereolithography, etc.) are currently being investigated for the fabrication of ceramic parts.^{7,9} Among these, robocasting (also called “Direct Ink Writing”-DIW) is emerging as a very promising, and conceptually simple, method. In robocasting, a green ceramic body is prepared through the continuous

extrusion of a ceramic paste (or ink).¹⁰ After printing, the green body is dried, de-bindered and sintered to form a dense ceramic.¹¹ However, the practical application of ceramic additive manufacturing faces several challenges. One of them is the need for reliable methodologies for building complex devices and composites combining different materials. Although in direct ink writing this can be achieved by combining more than one printhead or switching feeding systems, the process is not a simple one and the range of geometries that can be printed is limited.¹²

Embedded 3D printing is an emerging variant of robocasting based on the printing of a complex structure inside a soft supporting matrix.¹³ It has been successfully used to build vascular networks in hydrogels by printing sacrificial channels,^{9,14} to insert sensors in polymers,^{15,16} and to fabricate ceramic parts with complex shapes by using the matrix as a sacrificial support that is subsequently eliminated.^{17–22} Here, we have developed embedded printing so as to print complex structures inside dense ceramics. The requirements are more stringent than those for embedded printing in organic systems or when the matrix is merely a support. We have formulated a self-healing ceramic gel that enables the printing nozzle to move within while extruding a paste. The gel maintains the weight of the inserted printed parts (significantly denser than a polymer) and heal completely after the printing nozzle has passed. After drying and sintering it forms a dense, defect-free ceramic that encapsulates the printed structure. In addition, this printed structure should reproduce the design without distortion. To achieve these goals, it is necessary to match the viscoelastic behavior of matrix and ink and to control the post-printing process.

We demonstrate the potential of the embedded printing technique with two distinct examples in aluminum oxide; one in which the structure we print (steel) is denser than the matrix and the other where it is less dense (graphite). In the first case, we print a range of internal reinforcing framework structures from unidirectional fibre arrays to auxetic with the aim of increasing the fracture energy. In the second example, the graphite structure is subsequently eliminated to form complex microchannel arrays in alumina and build microfluidic devices. Our results suggest that embedded printing could be a viable alternative for the fabrication of a wide range multi-material ceramic matrix structures.

Results And Discussion

Embedded printing process optimisation

The embedded printing process is described in Fig. 1a and can be visualized in the supplementary information (supplementary video 1). In our system, both ink and matrix are based on Pluronic 127® gels containing inorganic powders. Pluronic has a triblock structure comprising hydrophilic PEO and hydrophobic PPO groups in a 2:1 ratio (Fig. 1b).¹⁰ Pluronic suspensions undergo gelation, accompanied by a three orders of magnitude increase in viscosity, above a critical transition temperature (Fig. 1c). The viscosity and the transition temperature are largely defined by the Pluronic concentration and the volume fraction of inorganic powder.²³ To warrant the formation of dense/defect free materials after drying and

sintering, the inorganic content of the gels used in the matrix and inks has to be relatively high. All our gels have powder contents above 25 vol%.

The matrix gel is cast into a silicone mold placed on tray at a temperature close to 0°C. At this temperature, the suspension can flow easily and fill the mold. Subsequently, the temperature is raised and continuously monitored until it reaches the desired value for printing (Fig. 1a). At this point, the printing nozzle is inserted into the gel and is held there for a few seconds until the matrix recovers its stiffness (Fig. 1d). Then the nozzle moves along the pre-programmed path while extruding the ink. Once the printing nozzle has passed, the matrix flows back to heal the gap left by the nozzle recovering its strength and stiffness to support the printed structure. Complete matrix healing is required in order to form a dense, defect-free ceramic after sintering. At the same time, the printed part should not displace or distort under the effects of gravity, \vec{F}_g , buoyancy, \vec{F}_b , or capillary forces. Using this approach, we have built a series of steel and graphite structures inside dense alumina (Fig. 1e-h).

The print fidelity and resolution depend on a delicate interplay between the viscoelastic properties of matrix and ink. To meet the requirements, the rheology of a matrix containing 37 vol% Al₂O₃ in 25wt% Pluronic gel was manipulated by controlling the printing temperature (Fig. 2a). Its behavior can be described using the Herschel-Bulkley equation (Fig. 2b):

$$\tau = \tau_y + K\dot{\gamma}^n \quad \text{Eq 1}$$

where τ is the applied stress, $\dot{\gamma}$ the shear rate, τ_y is the shear yield stress, n is the shear thinning coefficient and K is the viscosity parameter.²⁴ At all temperatures, the matrix exhibits shear thinning behavior, with $n < 1$ and K increasing with temperature (Table S1). The flow ramps also show hysteresis. The static yield stress, τ_y^{Stat} , measured when raising the shear rate, is higher than the dynamic one, τ_y^{Dyn} , recorded for a decreasing shear rate. Both τ_y^{Stat} and τ_y^{Dyn} increase with temperature (Fig. 2c and Table S1).

To enable the omnidirectional movement of the printing nozzle within it, the matrix structure should be broken at relatively low stresses (τ_y^{Stat}). As the nozzle passes, the internal friction of the matrix at the wake of the nozzle converts strain energy to thermal energy,²⁵ leading to hysteresis during reconstruction of the gel network. After the nozzle has passed, the matrix should flow to fully heal the gap left by it and recover enough strength (τ_y^{Dyn}) to hold the weight of the printed part.

To demonstrate the capabilities of embedded printing, inks containing two inorganic powders with very different densities (steel and graphite) were extruded in an alumina matrix. The powders were mixed with Pluronic gels to formulate pastes for extrusion. As with the matrix, the inks should have solid contents large enough as to form dense structures upon sintering and below the packing limit to facilitate extrusion (Fig. 2e_{iii} and Fig. S2).

All graphite and steel inks exhibit a shear thinning behavior with shear thinning coefficients in the range of 0.2–0.4. The inks also exhibit hysteresis in the flow measurements with $\tau_y^{Stat} > \tau_y^{Dyn}$ (Table S1). After the filaments are extruded in the Al_2O_3 matrix, they can move downward or upwards depending on the balance between gravity $\vec{F}_g = \rho_{ink} \vec{g} \pi r^2 L$ and buoyancy $\vec{F}_b = -\rho_{matrix} \vec{g} \pi r^2 L$, where ρ_{matrix} is the density of matrix suspension, ρ_{ink} is the density of ink suspension, \vec{g} is the acceleration of gravity, r is the radius of the ink filament and L is its length. The maximum stress that the matrix can apply on the circumference of ink filaments against their displacement or distortion and prevent the horizontal filaments from sinking or floating is equal to the yield stress of the matrix. The minimum yield stress required to avoid filament displacement could be estimated as:

$$\rho_{matrix} g \pi r^2 L \pm 2 r \tau_{y,matrix}^{dyn} L \geq \rho_{ink} g \pi r^2 L \quad \text{Eq 2}$$

$$\tau_{y,matrix}^{dyn} \geq \left| \frac{1}{2} g (\rho_{ink} - \rho_{matrix}) \right|$$

where $\tau_{y,matrix}^{dyn}$ is the dynamic yield stress of the matrix. This minimum yield stress varies with the composition and its value for steel and graphite inks in Al_2O_3 matrices are summarized in Table S1. Filaments printed in a matrix with $\tau_{y,matrix}^{Dyn}$ below this minimum will float or sink. Below 15 °C, the yield stress of the matrix is below 10 Pa which means it cannot provide effective support for structures printed with a dense ink. Above 15 °C, $\tau_{y,matrix}^{Dyn} > 70$ Pa, and the matrix can hold the printed structure in place without distortion.

Healing of the gaps left by the nozzle depends on the balance between the hydrostatic pressure at the printing depth that will drive the flow to close them and the dynamic yield stress of the matrix that will resist that pressure. The gaps remain when τ_y^{Dyn} is higher than the hydrostatic pressure, therefore the minimum printing depth, h , to fully heal the gaps can be estimated as $h = \frac{\tau_y^{Dyn}}{\rho_{matrix} g}$. Considering the properties of our matrix, gaps can be completely healed with a printing depth larger than 3.6 mm below 17 °C and more than 12.5 mm above 17 °C.

The time that takes the matrix to recover its properties after being broken by the passing nozzle is also critical. It determines whether the printed part will have time to move and deform before the matrix is able to hold it. It can be evaluated by the response of storage modulus G' or viscosity as a function of time during recovery tests.^{18,26} At 10 °C, it takes more than 10 s for the matrix to fully recover (Fig. 2d); this is too long as it allows the printed filaments to sink or float before the matrix regains its strength. The recovery time decreases with rising temperature (Fig. 2c) being around 5 s between 15 °C and 17 °C and 4 s at 25 °C. For samples printed at the highest temperature, 25 °C, a gap appears between the printed

filament and the matrix (Fig. 2e_i and Fig. 2e_{ii}). The recovery of matrix to its gel-like properties is too fast to enable enough flow to heal the gap left by the nozzle. As a result, printing temperatures around the liquid-gel transition (10–17 °C) are used to achieve a defect-free matrix, while faithfully retaining the features of the printed structure.

The yield stress of the ink also determines its ability to retain its shape. Steel inks with a Pluronic content of 25 wt% lose their shape at the printing temperature because their τ_y^{Dyn} is too low (Fig. 2c and 2e_{iv}). By increasing the Pluronic fraction from 25 to 30 wt% the τ_y^{Dyn} of the ink becomes sufficient to print filaments that retain a circular cross-section (Fig. 2e_v). For graphite inks, τ_y^{Dyn} always exceeds the minimum yield stress required when the printing temperature is above 15°C, resulting in round microchannels in the Al₂O₃ matrix (Fig. 1h and Fig. 2e_{vi}). Filament rupture can also arise during embedded printing. It happens when the continuous filaments bead up and form droplets due to the Plateau-Rayleigh instability. However, this does not take place for the filament diameters used in this work (see SI for more information).

Case study 1: printing dense steel fibres

We have taken advantage of embedded 3D printing to introduce steel reinforcing structures into Al₂O₃. The filament diameter can range between ~ 260 µm to ~ 70 µm depending on the nozzle selection (Fig. 3a). X-ray computed tomography (CT) analysis of the sintered composites printed with a 410 µm nozzle shows that the embedded structures (unidirectional fibre arrays, woodpile and auxetic structures) retain the original design (Fig. 1e-g). Quantitative image analysis on the X-ray CT virtual slices shows that the volume fraction of steel is the highest in the woodpile structure (~ 28vol%), followed by the auxetic structure (~ 25vol%) and then by the unidirectional fibre array (~ 11vol%). These samples were used for mechanical testing. The embedded steel fibre has a distance of 0.7mm among unidirectional fibre arrays and 0.65mm for woodpile structures. Despite the filaments being squeezed in woodpiles structures, the radius of filaments is the same as that in unidirectional arrays, ~ 0.13 mm. The unit cell of the auxetic structures is 2.3 mm in length and 2.6 mm in width.

The equivalent bending strength of all steel-alumina composites is of the same order (Fig. 3b), between 155 ± 23 to 289 ± 48 MPa, with the unidirectional fibre array exhibiting the highest strength despite having the lowest steel volume fraction. The measured plane strain fracture toughness, K_{IC} , is also very similar with values of 3.3 ± 0.2 MPa m^{1/2} for pure alumina and up to 4.0 ± 0.9 MPa m^{1/2} for steel composites. This is likely because in each case the crack propagation always starts in the ceramic. The small increase in K_{IC} for the composites could be due to the introduction of compressive residual thermal stresses in the matrix. We used a FEM thermomechanical model to estimate the magnitude of the residual stresses. After cooling, the compressive residual stresses in the ceramic matrix perpendicular to the loading direction can reach values up to 600 MPa (Fig. 3g, h and Fig. S3). However, the fracture behavior is very different from monolithic alumina and the architecture of the steel reinforcement plays a significant role. Whereas the ceramic demonstrates brittle failure, parts reinforced with unidirectional fibre arrays and

woodpile structures show progressive failure with a work of fracture up to $\sim 3 \text{ kJ/m}^2$. This is two orders of magnitude larger than the fracture energy estimated for our unreinforced alumina, $\sim 30 \text{ J/m}^2$ according to $G_{IC} = \frac{K_{IC}^2}{E}$. Upon bending the embedded auxetic steel framework shows a relatively extended plateau in the stress vs strain curve resulting in a further ($\sim 50\%$) improvement the work of fracture, reaching a value of 4.6 kJ/m^2 (Fig. 3c).

To monitor how the fracture propagates in these composites, in situ bending tests were carried out in the SEM and in the X-ray CT scanner. The unidirectional fibre array and woodpile structures show similar toughening mechanisms, primarily fibre bridging and plastic deformation of the steel (Fig. 3d). In samples having the woodpile reinforcement (Fig. 3e and Fig. S4), the cracks propagate along the interface between steel fibres (oriented parallel to crack propagation) and the Al_2O_3 , while the steel fibres perpendicular to the crack plane deform plastically locally and fracture.

The fracture behavior of the Al_2O_3 reinforced with an auxetic structure is more complex (Fig. 3f). As in the other steel-reinforced ceramics the main contributor to the fracture energy is the plastic deformation of the steel. The auxetic structure seems to maximize this contribution as the whole steel lattice plastically deforms significantly before fracturing at the nodes (Fig. 3f) while for the unidirectional fibre structure, steel plasticity is confined to the regions near the crack (Fig. 3d). In part this could be the result of the crack paths guided by the distribution of residual stresses that are tensile (50–180 MPa) in the regions close to the convex corners of the steel cells and gradually become slightly compressive, up to 50 MPa, at the center of the cell (Fig. 3h). High compressive stresses (100–650 MPa) also develop close to the concave corners. The auxetic structure directs the propagating crack along the interface between the steel and Al_2O_3 towards the corners of the cells where they are arrested (Fig. S5). Once the crack is arrested, further bending triggers extensive plastic deformation in the metal. In addition, the stresses in the auxetic structure promote crack branching and multiple arrest points that contribute to increased plastic deformation and the overall work of fracture.

Case Study 2: Printing sacrificial graphite filaments

Embedded 3D printing can also be used to introduce microchannels having a variety of complex three dimensional geometries into ceramic bodies in one simple step, without the need for laser cutting²⁷ or washing a prefabricated template.²⁸ Here, we print sacrificial graphite filaments in an Al_2O_3 matrix and the microchannels are then formed by the burn-out of carbon during sintering. We use the method to create straight microchannel arrays (Fig. 4a) and spiral microchannels (Fig. 1h). The cross section of the channels is circular with a diameter around $200 \mu\text{m}$ after sintering when printing at 15°C (Fig. 2e_{vi}), whereas droplet-shaped cross sections (Fig. 2e_{ij}) form above 15°C due to mismatch between the viscoelastic properties of the matrix and the ink. The effect of the distance between filaments was investigated by printing filaments with separations of 2 mm and 0.5 mm with a $410 \mu\text{m}$ stainless steel cylindrical tip at $14\text{--}15^\circ\text{C}$ (Fig. 4b). The thickness of the wall between filaments can be reduced down to $\sim 50 \mu\text{m}$ (Fig. 4b_{ij}). However, if the filaments become closer, they deform. This arises from the velocity

field generated in the Herschel-Bulkley fluid around the moving cylindrical tip.¹³ With a closer inter-filament distance, this velocity field affects the previously printed filaments and leads to deformation.

Channel connectivity is evident from the X-ray CT (Fig. 4a). The potential of such an arrangement is demonstrated by flowing cold water at a rate of 5.1 mL/min through a 21×10 channel array with the diameter of each channel ~ 200 µm (Fig. 4b) in an alumina cube (2.6×2.6×1.5 cm³) heated on a hot plate at 300°C (Fig. S6). Figure 4c shows the temperature change at the top surface of the Al₂O₃ cube. The temperature in the center falls from 119 °C to 62 °C in 200 seconds, consistent with good, continuous water flow (Supplementary video 2).

Conclusions

We have developed embedded 3D printing as a means of printing complex structures within dense ceramics. This is achieved by extruding ceramic inks inside a self-healing ceramic gel. In order to ensure high printing fidelity and the formation of a dense, defect-free material a number of conditions must be met:

- i. The viscoelastic response of the ink and the matrix gel must be matched to enable the matrix to support the embedded phase without significant movement
- ii. The matrix gel should break at low stresses to enable the movement of the nozzle in its interior and the extrusion of the ink.
- iii. The matrix gel must flow to ensure healing but recover its properties (stiffness and strength) fast enough to support the printed structure.
- iv. The ink should be extrudable but with a high dynamic yield stress to avoid deformation.
- v. Both matrix and inks should also have a high inorganic content to generate a dense, defect-free material after sintering.

To achieve these goals, we developed matrix and ink gels based on thermally reversible Pluronic hydrogels and manipulated their viscoelastic response by controlling the printing temperature, solid loading and Pluronic concentration. In particular, it was observed that for successful printing the temperature should be close to the liquid-gel transition of the matrix.

As a model to showcase the printing of complex shapes in a dense ceramic and to illustrate the benefits of the technique, we have used embedded printing to introduce steel and graphite structures within an alumina matrix. The diameter of the printed filaments ranges between 70 to 260 microns after sintering. The technique enables the introduction of embedded auxetic steel structures that generate fracture energies orders of magnitude above that of the ceramic and are significantly higher than those reached with grids or parallel fibre arrangements. The graphite can act as a sacrificial vehicle to create complex, three-dimensional microchannel arrays inside the ceramic. These results suggest that embedded printing is a viable alternative for the fabrication of multi-material inorganic structures and can open new opportunities for the design of composites and devices for structural and functional applications.

Experimental Section

Preparation of ink and matrix suspensions

Pluronic F127 powder (Sigma-Aldrich, UK) was dissolved in distilled water and stored in a fridge at 0 °C-4 °C for 24 h to obtain 25wt% and 30wt% Pluronic gels. Alumina (SMA6, Baikowski, France) with a d_{50} of 0.2 μm was sieved using a 100 μm plastic sieve in order to reduce the likelihood of agglomeration. The matrix slurry was prepared by adding the alumina powder to a 25wt% Pluronic gel in a weight ratio of 7:3. Dolapix CA was added as a dispersant, 1wt% with respect to the Al_2O_3 powder. This mixture was homogenized in a Thinky ARE-250 planetary mixer at 2000 rpm for 2 min, after chilling in an ice bath. The mixing and chilling steps were repeated for 3 to 5 times until a homogenous Al_2O_3 suspension was obtained with no remaining powder agglomerates. After the suspension was defoamed at 2200 rpm for 10 min to remove internal bubbles, it was cooled down below 13 °C and then gel cast in a silicone mould greased with silicone oil to facilitate mould release. An additional degassing step in a vacuum desiccator was performed to get rid of air trapped during gel casting.

The steel ink was prepared by mixing different volume ratios (25-40vol%) of steel powder (430L, 5 μm average particle size, US Research Nanomaterials, US) with a 25wt% or 30wt% Pluronic gel and adding 0.5wt% Dolapix to the mass of steel powder. The mixing and defoaming steps were the same as those mentioned above. The homogenous steel ink was placed in a 3 mL syringe barrel using a spatula and then transferred to another printing 3 mL syringe barrel using a syringe-syringe luer-lock connector to avoid trapping air. The graphite ink comprising a 30wt% Pluronic gel and graphite powder (7-11 μm particle size, 99%, Alfa Aesar, US) in a volume ratio of 3:1, was mixed and transferred to the syringe barrels in the same way as the steel ink.

Embedded Printing In A Ceramic Matrix

Printing patterns and parameters were defined using G-code for spiral structures and the remaining patterns with RoboCAD software (3dInks, USA). Steel and graphite fibres were printed using a robocaster system (3dInks, USA) with a printing speed of 6mm/s and stainless-steel tip nozzles with inner diameter of 0.15 mm (out diameter of 0.31 mm) and 0.41 mm (out diameter of 0.72 mm). The printing distance between steel and graphite filaments on the cross-section was varied from 0.5 mm to 3 mm. For mechanical tests, the bars with unidirectional steel fibre arrays, auxetic and woodpile structures were printed in Al_2O_3 matrices at 3mm/s. The temperature of the Al_2O_3 matrix suspension was adjusted between 10 °C and 18 °C by placing the silicone mould in an ice bath and measured whilst printing using a thermometer. A humidifier in the enclosure system was used to keep the humidity at $75\pm 10\%$ and inhibit water evaporation from the surface, which could cause crack formation of the final products.

Drying And Sintering

Drying was performed both in air and a high-humidity convection oven. The humidity in the oven, measured with a Thorlabs TSP01 sensor, was controlled at $72\pm3\%$ by placing a supersaturated NaCl solution inside. The temperature of this oven was set at $32\text{ }^{\circ}\text{C}$, and a fan was placed in it to promote air circulation. Drying lasted for 2–4 weeks, depending on the sample size. Dried samples were densified by cold isostatic pressing (CIP, Stansted Fluid Power LTD, UK) at 300 MPa for 5 min. To ensure that the Pluronic was gradually and completely burnt out without the generation of cracks, de-binding was first conducted in a chamber lift furnace with a heating rate of $1\text{ }^{\circ}\text{C}/\text{min}$ from room temperature to $350\text{ }^{\circ}\text{C}$ and held for 1h. After reaching $500\text{ }^{\circ}\text{C}$ with a heating rate of $2\text{ }^{\circ}\text{C}/\text{min}$, the temperature was maintained for 2h before cooling down. The steel reinforced Al_2O_3 composites were densified in a vacuum furnace by increasing the temperature to $600\text{ }^{\circ}\text{C}$ at a heating rate of $10\text{ }^{\circ}\text{C}/\text{min}$, before holding for 1h. After that, the temperature was raised to $1450\text{ }^{\circ}\text{C}$ using the same rate and maintained for 2h before cooling down to room temperature. In order to sinter the matrix and burn out the graphite in the Al_2O_3 /graphite to create microchannels, after de-binding at $500\text{ }^{\circ}\text{C}$ the samples were further sintered in a chamber lift furnace to $1550\text{ }^{\circ}\text{C}$ at a heating rate of $5\text{ }^{\circ}\text{C}/\text{min}$.

Rheological Measurements

The rheological behavior of matrix and ink suspensions was analyzed using a TA Instruments Discovery HR-1 rheometer with a 40mm parallel plate geometry and a $1000\text{ }\mu\text{m}$ gap. A few droplets of distilled water were placed on the solvent gap to prevent evaporation. The shear rate increased from 0.01 s^{-1} to 100 s^{-1} in 60 s during flow ramps and oscillatory tests were carried out from 1 to 2000 Pa at a fixed frequency of 1 Hz in amplitude sweeps. Hysteresis stress measurements were used to determine the yield stress to initiate ink flow and during the recovery. In the measurement, the shear rate went up from 0.01 s^{-1} to 100 s^{-1} and down to 0.01 s^{-1} . To simulate the Al_2O_3 matrix during printing and to monitor the matrix response as a function of time, a two-step modulus recovery test was performed by first increasing stress from 1 Pa to 1000 Pa and then keeping a low stress of 0.5 or 5 Pa. The recovery time was considered as the earliest point where storage modulus G' didn't obviously increase with time and the degree of recovery was calculated by dividing the storage modulus at the end by the initial storage modulus. Temperature ramp measurements were performed from $0\text{ }^{\circ}\text{C}$ to $40\text{ }^{\circ}\text{C}$ at a fixed shear rate of 1 s^{-1} .

Characterization

The microstructure of the as received powder and the polished sintered samples was observed using a JOEL 6010 SEM at 20 kV after a thin gold film was coated on the surface to improve conductivity. X-ray micro-computed tomography (CT) was used to investigate the internal structure of the Al_2O_3 . The as-printed Al_2O_3 with microchannels and steel-reinforced Al_2O_3 matrix composites were scanned using a Nikon Xtek High Flux Bay operating in a Zeiss Versa 520 X-ray microscope at 120kV and a power of 10W with 3179 projections recorded using a flat panel detector. The reconstructed volume had a voxel size of

5.4 μm . For the steel composite samples, the X-ray tube operated at 210 kV. This was combined with a 0.25 mm Cu energy filter to harden the X-ray beam. 2000 projections were recorded for each scan and the reconstructed volume had a voxel size of 11 μm . Image analysis was conducted using Avizo 9.3 software. The voxels representing the channels and steel reinforcements were picked out using region-growing and grey value thresholding. Dimensions of these features were determined from the segmented images. For microchannels, Al_2O_3 cubes as large as $2.6 \times 2.6 \times 1.5 \text{ cm}^3$ with multiple straight microchannels and $1.4 \times 1.4 \times 1.1 \text{ cm}^3$ with a spiral microchannel were printed with steel cylindrical tips.

Mechanical testing includes three-point bending to measure bending strength on polished samples with the tensile surfaces polished down to 1 μm and toughness using polished Single-Edge Notched Bend (SENB) samples ($25 \times 3 \times 3 \text{ mm}^3$ for composites with unidirectional arrays and woodpile structures and $25 \times 6 \times 3 \text{ mm}^3$ for composites with auxetic structures) according to ASTM E1820. The SENB specimens were notched with a 0.25 mm diamond wafering blade, the notch was sharpened with a razor blade and 1 μm diamond suspension. The tests were carried out on a Zwick iLine universal testing machine with a span of 15 mm at a displacement rate of 0.1 mm/min. Crack propagation during bending was observed in-situ using three-point bending tests in the SEM and four-point bending tests in X-ray CT. The SEM tests were performed in a MT300 Tensile Tester (DEBEN, UK) with a span of 21 mm. X-ray CT tests were performed in the Deben CT5000 with an inner span of 6 mm and an outer span of 20 mm. All in-situ tests used the same 0.1 mm/min displacement rate. The sample together with the rig was scanned using the Nikon Xtek High Flux Bay with the same settings used for the as-printed composites. The connectivity and cooling performance of the microchannels in Al_2O_3 were tested by flushing iced water through them. The iced water flux was controlled with a peristaltic pump (Watson Marlow SCI 400) at 5.1 mL/min and the temperature of the iced water and outlet tube was recorded. Temperature in the center of the Al_2O_3 was monitored from a top view with forward looking infrared camera (FLIR C2).

Finite Element Modelling Of Thermal Stress During Sintering

FEM of thermal stresses in steel/ alumina composites was conducted on the ABAQUS platform. The dimensions of sintered samples mentioned above were used and a symmetric boundary condition was applied to reduce the size of the modelling parts and allocate more meshes (150000–240000 C3D8R hexahedral elements). Plastic deformation of steel was considered for the calculation and parameters including Poisson's ratio, elastic modulus and plastic modulus were temperature-dependent,^{29,30} as listed in Table S2.

Declarations

Supporting Information

The Supporting Information is available from the online library or from the author.

Acknowledgements

This work was supported by the EPSRC Program Manufacture Using Advanced Powder Processes (MAPP)EP/P006566. S.Z. acknowledges financial assistance from the China Scholarship Council (No. 201806120001). This work was supported by the Henry Moseley X-ray Imaging Facility (funded through EPSRC grants EP/F007906/1, EP/F001452/1, EP/I02249X, EP/M010619/1, EP/F028431/1 and EP/M022498/1) within the Henry Royce Institute for Advanced Materials (funded through EPSRC grants EP/R00661X/1, EP/S019367/1, EP/P025021/1 and EP/P025498/1).

Author contributions

S.Z. performed the experiments and wrote the article. X.Z and P.W assisted in XCT scans. Y.H. and H.P. participated in the initial experimental exploration and studied in drying process. I.T., F.B., E.S guided the project, revised the content of article, and provided useful suggestions. All authors discussed the results and commented on the manuscript.

References

1. Hu, P. *et al.* Synthesis and characterization of ultralong SiC nanowires with unique optical properties, excellent thermal stability and flexible nanomechanical properties. *Sci Rep* **7**, 3011, doi:10.1038/s41598-017-03588-x (2017).
2. Cheng, Y. *et al.* One-step introduction of ZrC-SiC inside carbon fabric to fabricate high homogeneous and damage-tolerant composite inspired by vibration. *Journal of the European Ceramic Society* **39**, 2251–2256, doi:10.1016/j.jeurceramsoc.2019.02.030 (2019).
3. Du, B. *et al.* Ablation behaviors and mechanism of ultra-thick anti-oxidation layer coating on carbon-bonded carbon fiber composites. *Journal of the American Ceramic Society* **102**, 7543–7552, doi:10.1111/jace.16617 (2019).
4. Cheng, Y. *et al.* ZrB₂-Based "Brick-and-Mortar" Composites Achieving the Synergy of Superior Damage Tolerance and Ablation Resistance. *ACS Appl Mater Interfaces* **12**, 33246–33255, doi:10.1021/acsami.0c08206 (2020).
5. Muth, J. T. *et al.* Embedded 3D printing of strain sensors within highly stretchable elastomers. *Adv Mater* **26**, 6307–6312, doi:10.1002/adma.201400334 (2014).
6. Thakkar, H., Eastman, S., Al-Naddaf, Q., Rownaghi, A. A. & Rezaei, F. 3D-Printed Metal-Organic Framework Monoliths for Gas Adsorption Processes. *ACS Appl Mater Interfaces* **9**, 35908–35916, doi:10.1021/acsami.7b11626 (2017).
7. Feilden, E. *et al.* 3D Printing Bioinspired Ceramic Composites. *Sci Rep* **7**, 13759, doi:10.1038/s41598-017-14236-9 (2017).
8. Rödel, J. *et al.* Development of a roadmap for advanced ceramics: 2010–2025. *Journal of the European Ceramic Society* **29**, 1549–1560, doi:10.1016/j.jeurceramsoc.2008.10.015 (2009).

9. Wu, W., DeConinck, A. & Lewis, J. A. Omnidirectional printing of 3D microvascular networks. *Adv Mater* **23**, H178-183, doi:10.1002/adma.201004625 (2011).
10. Feilden, E., Blanca, E. G.-T., Giuliani, F., Saiz, E. & Vandeperre, L. Robocasting of structural ceramic parts with hydrogel inks. *Journal of the European Ceramic Society* **36**, 2525–2533, doi:10.1016/j.jeurceramsoc.2016.03.001 (2016).
11. Peng, E., Zhang, D. & Ding, J. Ceramic Robocasting: Recent Achievements, Potential, and Future Developments. *Adv Mater* **30**, e1802404, doi:10.1002/adma.201802404 (2018).
12. Smay, J. E., Nadkarni, S. S. & Xu, J. Direct Writing of Dielectric Ceramics and Base Metal Electrodes. *International Journal of Applied Ceramic Technology* **4**, 47–52, doi:10.1111/j.1744-7402.2007.02118.x (2007).
13. Grosskopf, A. K. *et al.* Viscoplastic Matrix Materials for Embedded 3D Printing. *ACS Appl Mater Interfaces* **10**, 23353–23361, doi:10.1021/acsami.7b19818 (2018).
14. Jennifer A. Lewis, D. B. K., Mark A. Skylar - Scott, Kimberly A. Homan, Ryan L. Truby, Amelia Sydney Gladman. Method of printing a tissue construct with embedded vasculature. (2018).
15. Truby, R. L. *et al.* Soft Somatosensitive Actuators via Embedded 3D Printing. *Adv Mater* **30**, e1706383, doi:10.1002/adma.201706383 (2018).
16. Wehner, M. *et al.* An integrated design and fabrication strategy for entirely soft, autonomous robots. *Nature* **536**, 451–455, doi:10.1038/nature19100 (2016).
17. Huang, K., Elsayed, H., Franchin, G. & Colombo, P. Embedded direct ink writing of freeform ceramic components. *Applied Materials Today* **23**, 101005, doi:https://doi.org/10.1016/j.apmt.2021.101005 (2021).
18. Mahmoudi, M., Burlison, S. R., Moreno, S. & Minary-Jolandan, M. Additive-Free and Support-Free 3D Printing of Thermosetting Polymers with Isotropic Mechanical Properties. *ACS Appl Mater Interfaces* **13**, 5529–5538, doi:10.1021/acsami.0c19608 (2021).
19. Mahmoudi, M. *et al.* Three-Dimensional Printing of Ceramics through "Carving" a Gel and "Filling in" the Precursor Polymer. *ACS Appl Mater Interfaces* **12**, 31984–31991, doi:10.1021/acsami.0c08260 (2020).
20. O'Bryan, C. S. *et al.* Three-dimensional printing with sacrificial materials for soft matter manufacturing. *MRS Bulletin* **42**, 571–577, doi:10.1557/mrs.2017.167 (2017).
21. Hinton, T. J., Hudson, A., Pusch, K., Lee, A. & Feinberg, A. W. 3D Printing PDMS Elastomer in a Hydrophilic Support Bath via Freeform Reversible Embedding. *ACS Biomater Sci Eng* **2**, 1781–1786, doi:10.1021/acsbiomaterials.6b00170 (2016).
22. Afghah, F., Altunbek, M., Dikyol, C. & Koc, B. Preparation and characterization of nanoclay-hydrogel composite support-bath for bioprinting of complex structures. *Sci Rep* **10**, 5257, doi:10.1038/s41598-020-61606-x (2020).
23. Vadnere, M., Amidon, G., Lindenbaum, S. & Haslam, J. L. Thermodynamic studies on the gel-sol transition of some pluronic polyols. *International Journal of Pharmaceutics* **22**, 207–218, doi:https://doi.org/10.1016/0378-5173(84)90022-X (1984).

24. Herschel, W. H. & Bulkley, R. Konsistenzmessungen von Gummi-Benzollösungen. *Kolloid-Zeitschrift* **39**, 291–300, doi:10.1007/BF01432034 (1926).
25. Smay, J. E., Cesarano, J. & Lewis, J. A. Colloidal Inks for Directed Assembly of 3-D Periodic Structures. *Langmuir* **18**, 5429–5437, doi:10.1021/la0257135 (2002).
26. Corker, A., Ng, H. C., Poole, R. J. & Garcia-Tunon, E. 3D printing with 2D colloids: designing rheology protocols to predict 'printability' of soft-materials. *Soft Matter* **15**, 1444–1456, doi:10.1039/c8sm01936c (2019).
27. Therriault, D., Shepherd, R. F., White, S. R. & Lewis, J. A. Fugitive Inks for Direct-Write Assembly of Three-Dimensional Microvascular Networks. *Advanced Materials* **17**, 395–399, doi:10.1002/adma.200400481 (2005).
28. Kotz, F. *et al.* Fabrication of arbitrary three-dimensional suspended hollow microstructures in transparent fused silica glass. *Nat Commun* **10**, 1439, doi:10.1038/s41467-019-09497-z (2019).
29. Auerkari, P. *Mechanical and physical properties of engineering alumina ceramics*. Vol. 23 (Technical Research Centre of Finland Espoo, 1996).
30. Fukuhara, M. & Sanpei, A. Elastic moduli and internal friction of low carbon and stainless steels as a function of temperature. *ISIJ international* **33**, 508–512 (1993).

Figures

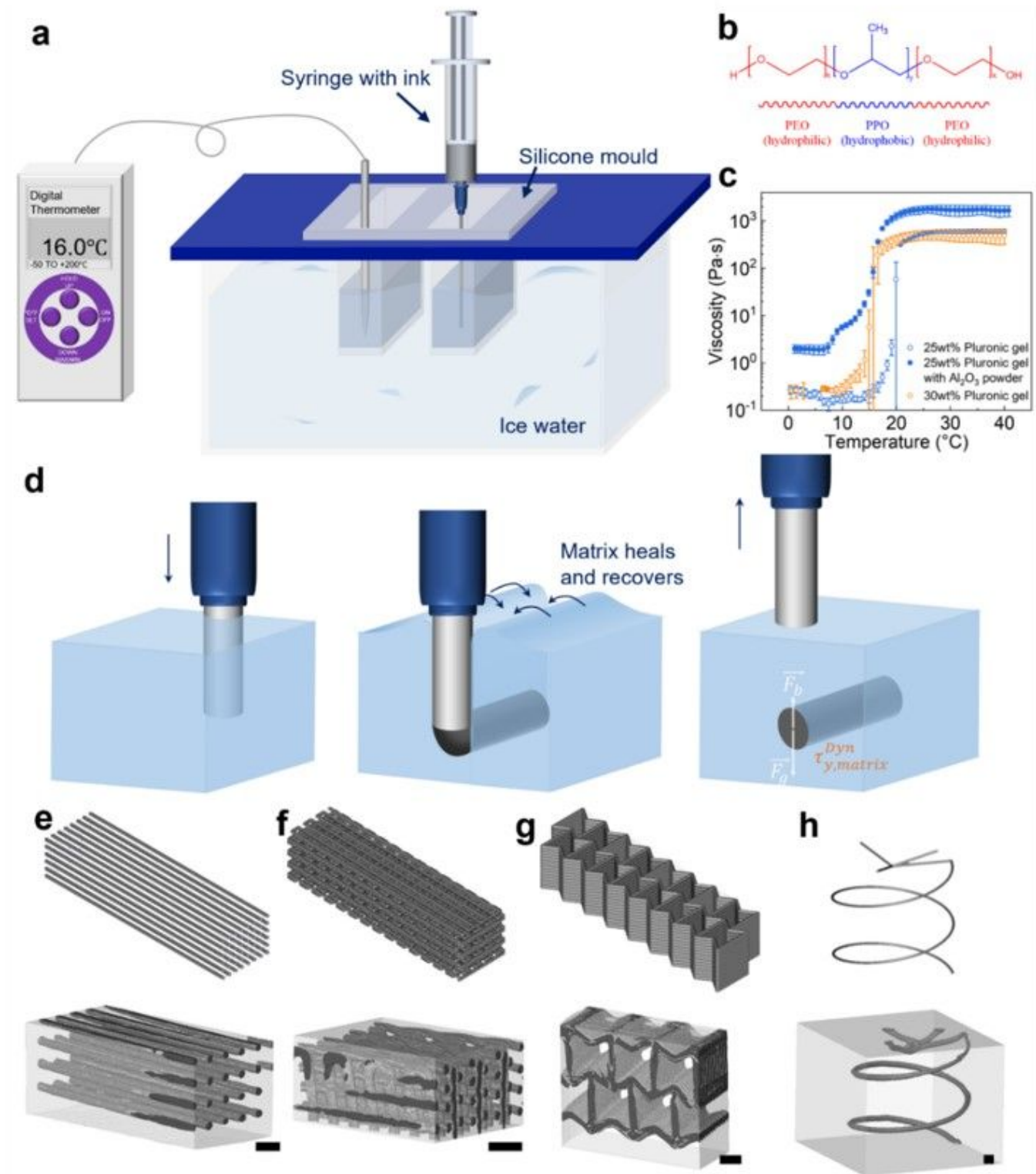


Figure 1

(a) Schematics of embedded 3D printing. The matrix suspension is gel-casted in a silicone mold and the ink suspensions extruded according to a CAD model. (b) Chemical structure of Pluronic F127® (c) Viscosity-temperature curve of 25wt% and 30wt% Pluronic gel and the gel with inorganic powder (d) Illustration of the embedded printing process. First, the nozzle tip goes into the matrix suspension and then travels according to CAD models as the ink is being extruded. The matrix behind the nozzle flows

back to heal the gap and finally the nozzle is removed after the whole structure is printed and sustained in the position. (e-h) CAD models (top) and the 3D X-ray CT images (bottom) of the steel and microchannel structures (rendered dark grey) embedded in Al_2O_3 matrices (rendered light grey), scale bar 1mm (e) unidirectional steel fibre array (f) steel woodpile structure (g) steel auxetic structure (h) spiral channel with three inlets in Al_2O_3 .

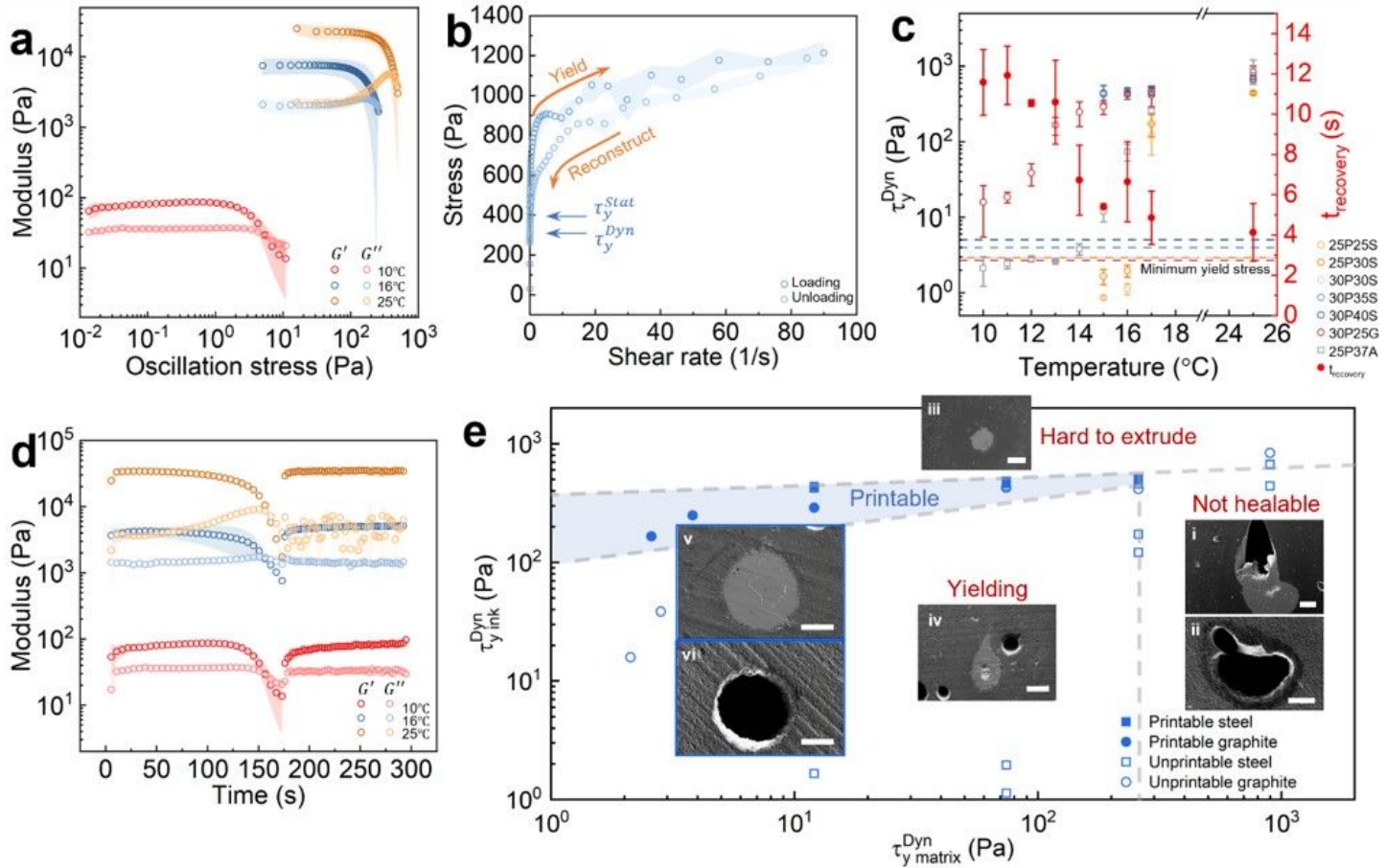


Figure 2

(a) Oscillatory test of Al_2O_3 matrix suspension at 10-25 °C (b) Illustration of hysteresis stress measurement of Al_2O_3 matrix suspension at 17 °C. (c) Recovery time of Al_2O_3 matrix printable (solid symbols) and dynamic yield stress of the matrix and inks (open symbols) as a function of temperature. The minimum yield stress depending on the density of the ink (Eq. 2) is labeled with dashed lines in the color corresponding to the ink composition. The notation describes the Pluronic and solid content with S for steel, G for graphite and A for alumina. For example, 25P25S represents 25wt% Pluronic 25vol% steel. (d) Two-step modulus recovery tests of the Al_2O_3 matrix. (e) Dynamic yield stress of printable (solid symbols) and not printable (open symbols) combinations of ink and matrix suspensions in this work. SEM images of not printable combination of ink and matrix suspensions. i. 30P30S filaments printed in Al_2O_3 matrix at 17-18 °C ii. 30P25G filaments printed in Al_2O_3 matrix at 16-17 °C iii. 30P40S filaments printed in Al_2O_3 matrix iv. 25P25S filaments printed in Al_2O_3 matrix at 15-16 °C. SEM images of printable

combination of ink and matrix suspensions. v. 30P30S filaments printed in Al_2O_3 matrix at 16 -17 °C vi. 30P25G filaments printed in Al_2O_3 matrix below 15 °C, scale bar 100 μm .

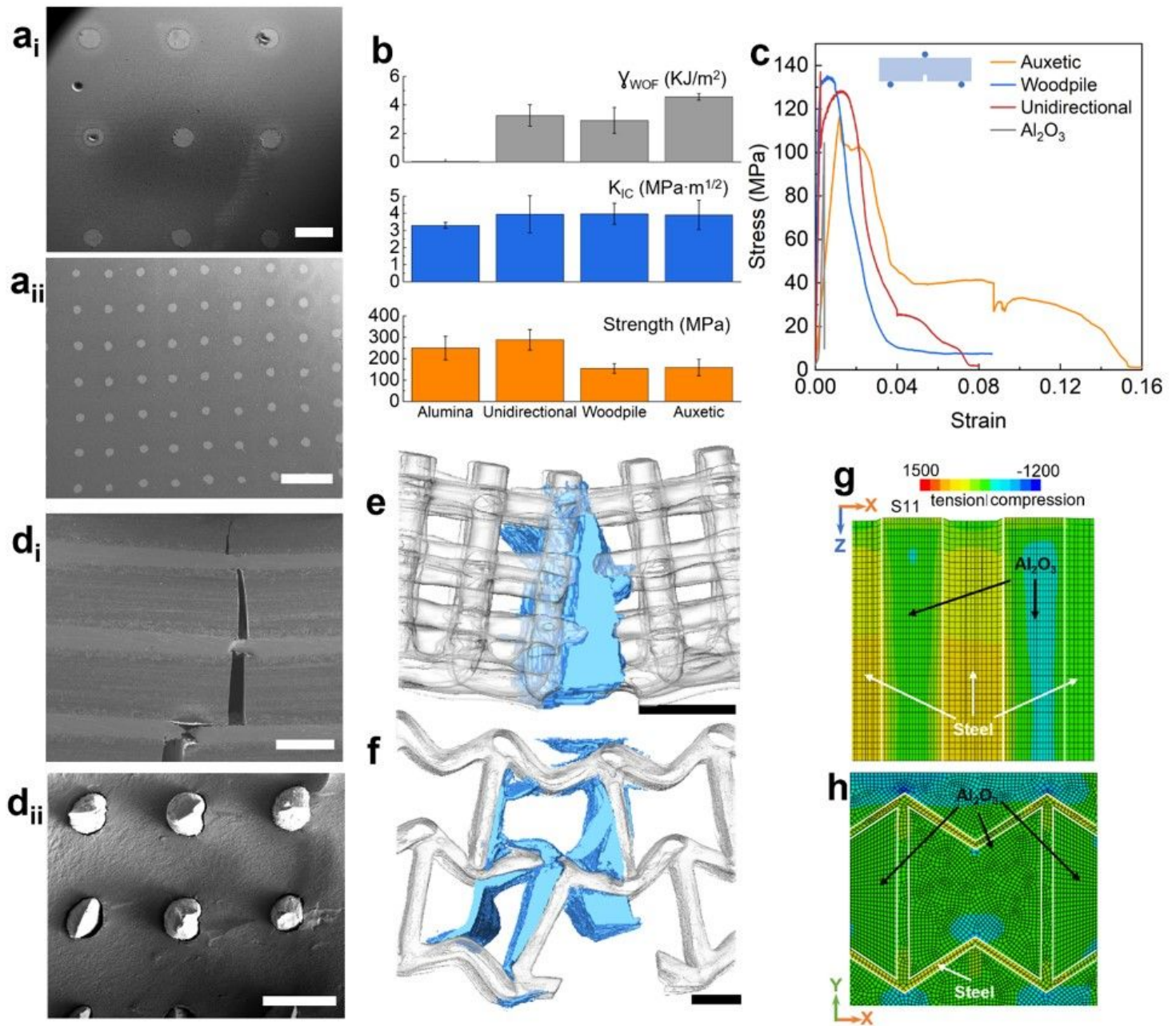


Figure 3

(a) Steel unidirectional arrays in Al_2O_3 printed with a i) 410 μm nozzle (filament diameter $\sim 260 \mu\text{m}$ after sintering) and ii) 150 μm nozzle (filament diameter $\sim 70 \mu\text{m}$ after sintering), scale bar 500 μm . (b) Strength, toughness and work of fracture of Al_2O_3 and its composites (c) Stress-strain curve of Al_2O_3 and its composites (d) i) longitudinal SEM image of unidirectional composite during 3-point bending and ii) its fracture surface, scale bar 500 μm . Volume X-ray CT renderings of the e) steel woodpile and f) auxetic structures with the ceramic rendered transparent the crack blue and the framework light grey during in-situ 4-point bending, scale bar 1mm. Finite element modelling of thermal stress introduced cooling from

the sintering temperature for g) woodpile and h) auxetic structures reinforced Al_2O_3 composites, unit of stress MPa.

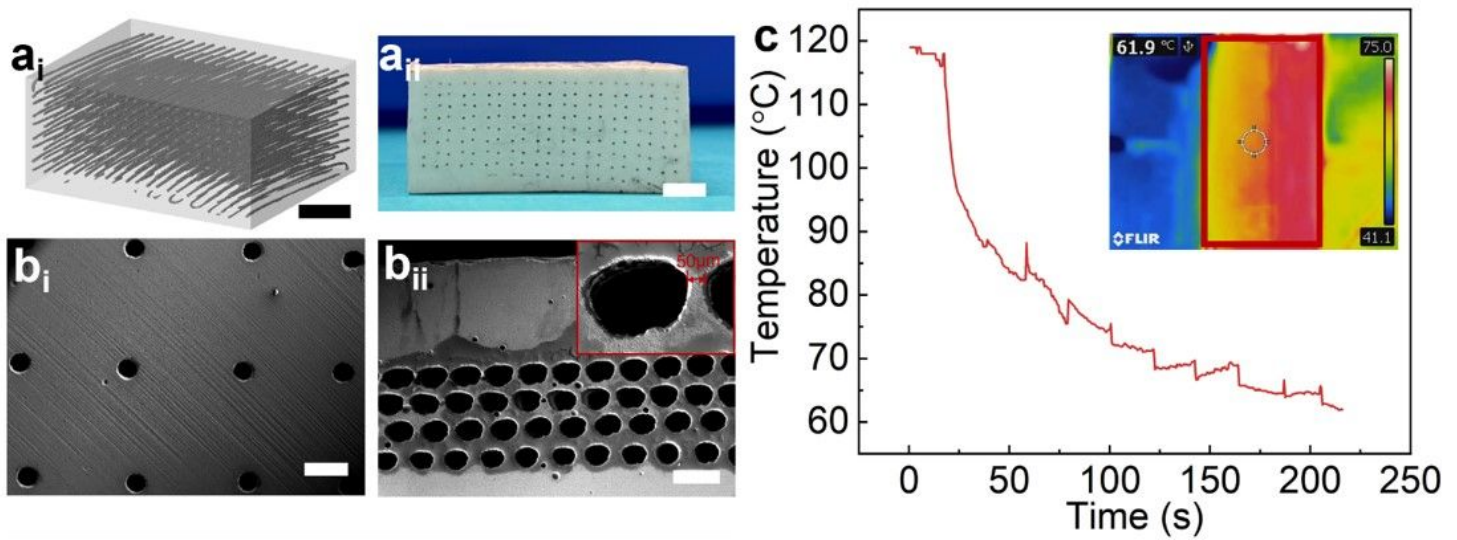


Figure 4

(a) i) 3D X-ray CT volume rendering and ii) and a cross-section of a large Al_2O_3 cube with straight microchannels printed with 0.41 mm stainless steel tip, scale bar 5 mm (b) 200mm diameter microchannels in Al_2O_3 printed with i) 2mm and ii) 0.5mm spacings, scale bar 500 μm (c) The change in temperature on the surface of Al_2O_3 microchannel cube upon flushing cold water through the channels (fluctuations are due to the infrared camera being calibrated every 25 seconds). Insert: the thermal images of Al_2O_3 (labelled with the red box) and clamps from the top after cooling.

Supplementary Files

This is a list of supplementary files associated with this preprint. Click to download.

- [SupplementaryInfo.pdf](#)
- [supplementaryvideo1.mov](#)
- [supplementaryvideo2.avi](#)